

Self-Supervised Coordinate Projection Network for Sparse-View Computed Tomography

Qing Wu, Ruimin Feng, Hongjiang Wei, *Member, IEEE*, Jingyi Yu, *Fellow, IEEE*,
and Yuyao Zhang, *Member, IEEE*

Abstract—In the present work, we propose a Self-supervised COordinate Projection nEtwork (SCOPE) to reconstruct the artifacts-free CT image from a single SV sinogram by solving the inverse tomography imaging problem. Compared with recent related works that solve similar problems using implicit neural representation network (INR), our essential contribution is an effective and simple re-projection strategy that pushes the tomography image reconstruction quality over supervised deep learning CT reconstruction works. The proposed strategy is inspired by the simple relationship between linear algebra and inverse problems. To solve the under-determined linear equation system, we first introduce INR to constrain the solution space via image continuity prior and achieve a rough solution. And secondly, we propose to generate a dense view sinogram that improves the rank of the linear equation system and produces a more stable CT image solution space. Our experiment results demonstrate that the re-projection strategy significantly improves the image reconstruction quality (+3 dB for PSNR at least). Besides, we integrate the recent hash encoding into our SCOPE model, which greatly accelerates the model training. Finally, we evaluate SCOPE in parallel and fan X-ray beam SVCT reconstruction tasks. Experimental results indicate that the proposed SCOPE model outperforms two latest INR-based methods and two well-popular supervised DL methods quantitatively and qualitatively.

Index Terms—Sparse-View Computed Tomography, Inverse Imaging Problem, Self-Supervised Learning, Implicit Neural Representation

I. INTRODUCTION

X-RAY Computed Tomography (CT) is widely applied in clinical diagnosis, industrial non-destructive testing, and safety inspection [1], [2]. In the recent several years, CT played a critical role in the auxiliary diagnosis and disease course monitoring of COVID-19 pneumonia [3]. However, the high-level radiation exposure caused by longitudinal frequent CT scans may increase the lifetime risk of cancer, especially for patients undergoing disease monitoring via CT scans such as pneumonia and cancer [4], [5]. Therefore, reducing the radiation exposure to CT imaging is an urgent need for the current public health status.

Qing Wu and Jingyi Yu are with School of Information Science and Technology, ShanghaiTech University, Shanghai, China (e-mail: {wuqing, yujingyi}@shanghaitech.edu.cn).

Ruiming Feng and Hongjiang Wei are with School of Biomedical Engineering and Institute of Medical Robotics, Shanghai Jiao Tong University, Shanghai, China (e-mail: {Fengruimin, hongjiang.wei}@sjtu.edu.cn).

Yuyao Zhang (Corresponding Author) is with School of Information Science and Technology and iHuman Institute, ShanghaiTech University, Shanghai, China (e-mail: zhangyy8@shanghaitech.edu.cn).

Mathematically, the CT acquisition process can be formulated as a linear forward model:

$$\mathbf{y} = \mathbf{A}\mathbf{x} + \mathbf{n}, \quad (1)$$

where $\mathbf{y} \in \mathbb{R}^{N_y}$ is the measurement data (also known as sinogram), $\mathbf{x} \in \mathbb{R}^{N_x}$ denotes the CT image to be constructed, $\mathbf{A} \in \mathbb{R}^{N_y \times N_x}$ represents the CT system forward imaging model (e.g., Radon transform operator for parallel X-ray beam CT), and $\mathbf{n} \in \mathbb{R}^{N_y}$ is the system noise. To reduce the imaging radiation dose, one can decrease the dimension of measurement data, denoting as \mathbf{y}_s , an undersampling of sinogram \mathbf{y} . To reconstruct a CT image from the under-sampled sinogram \mathbf{y}_s is referred to as Sparse-View (SV) CT reconstruction, a highly ill-posed under-determined inverse imaging problem. Using analytical reconstruction algorithms, such as Filtered Back-Projection (FBP) [10] on the SV sinogram \mathbf{y}_s , results in severe streaking artifacts in the constructed CT image.

To eliminate the streaking artifacts, conventional machine learning methods [11]–[14] formulate the under-determined inverse imaging as a regularized optimization problem. Explicit image prior assumptions (e.g., minimal Total Variation (TV) [14] for inducing smoothness in CT image) are adopted as a regularization term to restrict the search space and promote desired consistent image solutions [15]. Recently, supervised Deep Learning (DL) methods [16]–[22] have shown great potential for SVCT reconstruction. Instead of directly solving the inverse imaging problem, a supervised DL reconstruction mostly employs Convolutional Neural Network (CNN) to learn an end-to-end mapping from low-quality images to their high-quality reconstruction over a large dataset. For example, [16] proposed FBPCNN that trains a U-Net [23] to learn a residual from artifacts-corrupted inputs to artifacts-free outputs. It is known that the performance of the supervised DL methods mostly depends on the scale and data distribution of the image pairs in the training dataset (i.e., a large-scale training dataset that covers more types of variations generally provides better performance). However, it is very challenging to build a comprehensive training dataset that includes all variable influencing factors on SVCT images, such as different levels of SV undersampling, different beam types for measurement data projection, imaging for different body tissue and other unlimited conditions. For real clinical applications, supervised DL methods performance might be quite limited and even fail in extreme cases (e.g., rare disease-caused image patterns) that are not covered by the training dataset.

Implicit Neural Representation (INR) has recently been proposed to model and represent 3D scenes from a sparse

TABLE I
COMPARISON OF THE PROPOSED SCOPE WITH EXISTING INR-BASED SVCT RECONSTRUCTION METHODS.

Methods	Key Factors for SVCT	Input	Output	Learning Target	Main Objective	Encoding Strategy
GRFF [6]	INR Implicit Prior	SV sinogram \mathbf{y}_s	CT image $\hat{\mathbf{x}}$	CT image $f_{\Theta} : (x, y) \rightarrow \mathbf{x}$	$\arg \min_{\Theta} \mathcal{L}(\mathbf{A}f_{\Theta}, \mathbf{y}_s)$	Fourier encoding
IntroTomo [7]	INR Implicit Prior + Explicit Prior	SV sinogram \mathbf{y}_s	CT image $\hat{\mathbf{x}}$	CT image $f_{\Theta} : (x, y) \rightarrow \mathbf{x}$	$\arg \min_{\Theta} \mathcal{L}(\mathbf{A}f_{\Theta}, \mathbf{y}_s)$	Fourier encoding
NeRP [8]	INR Implicit Prior	A prior CT image + SV sinogram \mathbf{y}_s	CT image $\hat{\mathbf{x}}$	CT image $f_{\Theta} : (x, y) \rightarrow \mathbf{x}$	$\arg \min_{\Theta} \mathcal{L}(\mathbf{A}f_{\Theta}, \mathbf{y}_s)$	Fourier encoding
CoIL [9]	DV Sinogram Generation	SV sinogram \mathbf{y}_s	DV sinogram $\hat{\mathbf{y}}_d$	Sinogram $g_{\Theta} : (\theta, \rho) \rightarrow \mathbf{y}$	$\arg \min_{\Theta} \mathcal{L}(g_{\Theta}, \mathbf{y}_s)$	Linear encoding
SCOPE (Ours)	INR Implicit Prior + DV Sinogram Generation	SV sinogram \mathbf{y}_s	DV sinogram $\hat{\mathbf{y}}_d$	CT image $f_{\Theta} : (x, y) \rightarrow \mathbf{x}$	$\arg \min_{\Theta} \mathcal{L}(\mathbf{A}f_{\Theta}, \mathbf{y}_s)$	Hash encoding

set of 2D views using coordinate-based deep neural networks in a self-supervised fashion. The core component in INR is a continuous implicit function parameterized by a Multi-Layer Perceptron (MLP). Benefiting from the image continuity prior imposed by the implicit function and the neural network architecture, INR has achieved superior performance in various vision problems (*e.g.*, surface reconstruction [24]–[26], view synthesis [27]–[29], and image super-resolution [30], [31]).

For SVCT imaging, an early attempt by [6] indicated that INR could be applied to recover the CT image from a single SV sinogram without using any external data. Since then, more INR-based works [7]–[9], [32] have been emerged. We summarize the recent works that solve the tomography imaging inverse problem using INR-based methods in Table I to compare the design ideas and characteristics of various methods more clearly. [9] proposed CoIL that trains an INR to represent the SV sinogram and predicts the accordance Dense-View (DV) sinogram based on the continuous nature of INR. The CT image reconstruction is then processed by applying FBP [10] on the DV sinogram. However, the coordinate space of sinogram does not follow the intuitive orthogonal assumption of Fourier spacial encoding in INR model. Thus the CT reconstruction performance of CoIL is limited and not comparable with supervised methods. NeRP [8] proposed to utilize a series of longitudinal CT scans of the same subject to build CT image from SV sinogram. The INR is firstly trained in advance on a prior CT scan, and then used as image prior to recover high-quality CT images from the rest SV sinograms. However, longitudinal CT scans are not always available, which may limit the model application scenario. [7] proposed IntroTomo consists of a sinogram prediction module and a geometry refinement module, which are applied iteratively. The former estimates the CT image from the SV sinogram, while the latter combines explicit priors (TV and Non-local Mean) into an optimization framework to refine CT images. The iterative training strategy produces elevation in CT image quality but severely prolongs reconstruction time.

Compared with the works in Table I, the proposed method is most related to [6], [9]. However, there are two major limitations unsolved in those works: (i) The INR estimated the desired CT image by minimizing the loss between the network predicted sinogram and the real measured sinogram. Thus the paradigm is more efficient in sinogram generation but not in CT image reconstruction. Due to the highly sparse sinogram, the MLP tends to approach an implicit function

that overfits the SV sinogram, which manifests as noisy INR represented CT images; (ii) Due to the heavy computation of the coordinate-based based deep MLP, the image-specific INR based CT reconstructions generally performs poorly on time-efficiency.

In this paper, we propose a Self-supervised COordinate Projection nEtwork (SCOPE) to reconstruct the artifacts-free CT image from a single SV sinogram by solving the inverse tomography imaging problem. Compared with existing related works [6], [7], one of our key contributions is a simple and effective re-projection strategy that significantly improves the reconstruction quality of tomography images. This strategy is inspired by the simple relationship between linear algebra and inverse problems. We consider the SVCT inverse imaging problem as an under-determined system of linear equations. The total number of X-rays involved in all sinogram is equivalent to the number of independent linear equations (*i.e.*, the rank of matrix \mathbf{A} in Equation 1). Thus the number of free variables in the linear equations largely increases with the decrease of matrix \mathbf{A} 's rank in SV sinogram. By introducing INR, the solution space of image \mathbf{x} is efficiently constrained in a continuous space, inducing a satisfied inverse CT reconstruction from a highly sparse sinogram. However, this reconstruction is one unstable solution among infinite solutions that satisfy the acquired SV sinogram \mathbf{y}_s , which can be easily affected by network overfitting to the SV sinogram. For achieving a more stable solution, we propose the novel re-projection strategy to build a DV sinogram from this initial CT reconstruction. This process is equivalent to generating a higher rank linear equations system for presenting the inverse imaging task, which assist us to find a more stable solution with much fewer free variables in the CT image. Our experiment results demonstrate that through the re-projection strategy, we can further suppress the image noise while preserving the image details in the resulting CT images, which significantly improves the image reconstruction quality (+3 dB for PSNR at least). In addition, learning high-frequency signals via simple MLP is practically very difficult due to the spectral bias problem [33], [34]. Existing INR-based methods mostly combine pre-defined encoding modules (*e.g.*, Fourier encoding in [6]) with a deep MLP to learn the implicit function, which results in heavy computational cost. To accelerate the model training, we integrate the recent hash encoding [35] into our SCOPE model, enabling shallow (three-layers) MLP achieve superior fitting ability (1 minute). We conduct extensive ex-

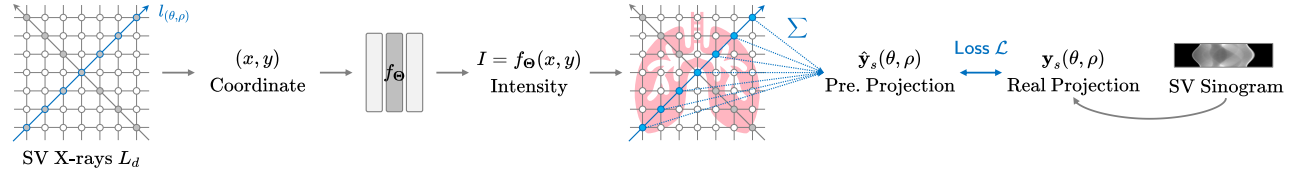
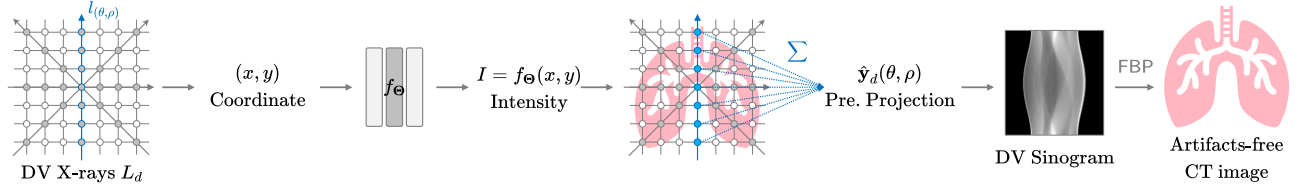
A. Learning Implicit Function

B. Re-projection Reconstruction


Fig. 1. Workflow of the proposed SCOPE model.

periments on two publicly datasets (AAPM and COVID-19) for model evaluation. Both qualitative and quantitative results indicate that SCOPE outperforms two most recent INR-based methods (CoIL and GRFF [6]) and two well-known supervised CNN-based models (FBPConvNet [16] and TF U-Net [17]). To our best knowledge, the proposed SCOPE is the first self-supervised method that outperform the supervised DL models for SVCT reconstruction. The main contributions of this work are summarized as below:

- 1) We propose SCOPE that recover the high-quality CT image from single SV sinogram without involving any external data.
- 2) We propose a simple and effective re-projection reconstruction strategy that significantly improve the resulting CT image quality.
- 3) We integrate the hash encoding [35] into our SCOPE, which greatly accelerates the model training and thus improves the model practicability.
- 4) We conduct extensive experiments, and the results indicate that our SCOPE outperforms two latest INR-based methods and two well-known supervised DL methods, quantitatively and qualitatively.

II. METHODOLOGY
A. Model Overview

In the proposed SCOPE model, we represent the desired CT image \mathbf{x} as a continuous function parameterized by a neural network:

$$I = f_{\Theta}(x, y), \quad (2)$$

where Θ denote the trainable parameters (weights and biases) of the network, $(x, y) \in \mathbb{R}^2$ is any 2D spatial coordinate in the imaging plane, and $I \in \mathbb{R}$ is the corresponding image intensity at the position (x, y) in the image \mathbf{x} . Based on the acquired SV sinogram \mathbf{y}_s , we then optimize the network to approximate the implicit function using back-propagation gradient descent algorithm to minimize the objective as below:

$$\hat{\Theta} = \arg \min_{\Theta} \mathcal{L}(\hat{\mathbf{y}}_s, \mathbf{y}_s), \quad \hat{\mathbf{y}}_s = \mathbf{A}f_{\Theta}, \quad (3)$$

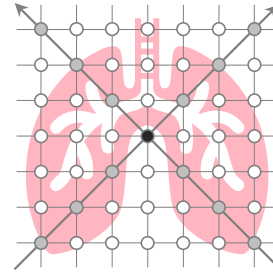


Fig. 2. A toy example of different types of sample points in SVCT: **Black** sample points are scanned by multiple X-rays, whose pixel intensities are well constrained in the inverse imaging problem; **Gray** sample points are scanned by a single X-ray; **White** sample points are not scanned by any X-ray. The gray and white points are examples of free variable pixels, whose intensities are not tightly constrained in the inverse problem.

where $\hat{\mathbf{y}}_s$ represents the predicted SV sinogram and \mathcal{L} is the loss function that measures the discrepancy between the predicted SV sinogram $\hat{\mathbf{y}}_s$ and the acquired SV sinogram \mathbf{y}_s .

The key insight behind Equation 3 is that using the image continuity prior imposed by the implicit function and the neural network architecture to regularize the inverse imaging problem of SVCT and thus obtaining the desired solution. After the network training, the optimal image $\hat{\mathbf{x}}$ is theoretically $f_{\hat{\Theta}}$. However, due to the highly under-determined inverse imaging problem, the network tends to approach an implicit function that overfits the SV sinogram \mathbf{y}_s and thus fails to approximate the desired implicit function well, which manifests as a lot of noises in the resulting CT image $\hat{\mathbf{x}} = f_{\hat{\Theta}}$.

To this end, we propose a re-projection reconstruction strategy, in which the learned function $f_{\hat{\Theta}}$ is used to generate a DV sinogram $\hat{\mathbf{y}}_d$. Then the final high-quality CT image $\hat{\mathbf{x}}$ is reconstructed by applying FBP [10] on $\hat{\mathbf{y}}_d$. An essential insight is that the INR network overfitting on the SV sinogram results in unexpected pixel intensity mutations in the CT image reconstruction. Figure 2 illustrates a toy example of different types of sample points in SV reconstructed CT. For example, the black sample points are scanned by multiple X-rays, which can be considered as constrained by multiple linear equations. Thus the INR network can accurately recover its

image intensity through the constraints of the cross projections. For the gray and white sample points scanned only by few, or even no X-rays, the pixel intensities are not tightly constrained in the inverse problem. Their pixel intensities are mostly approximated by the image continuity prior imposed by the implicit function, and are easily effected by the overfitting effected towards the sparse measurements of sinogram. Therefore, the learned function f_{Θ} may output pixel intensity mutation at those free variable positions due to the overfitting problem. Although these mutations manifests similarly to image noise, they do not follow any typical distribution, thus the performance of inserting common denoising regularization term is limited [7]. The most effective strategy to suppress free variable mutations is thus to generate a higher rank linear equation system that tightly constrain the pixel intensities in the CT image and produce the same solution space with the SV sinogram. The generation of a DV sinogram \hat{y}_d from f_{Θ} is thus proposed. The workflow of the proposed SCOPE model is shown in Figure 1.

B. Learning Implicit Function

Figure 1 A demonstrates the pipeline of learning implicit function by a neural network. Given a SV sinogram $\mathbf{y}_s \in \mathbb{R}^{K \times M}$, where K and M are the number of projection views and X-rays per view respectively, we first build a total number of $K * M$ X-rays L_s from the K sparse projection views (*i.e.*, M X-rays per view). Next, we feed the spatial coordinates (x, y) of sample points along the SV X-rays L_s into the implicit function to produce the corresponding image intensities $I = f_{\Theta}(x, y)$. Finally, we compute the predicted projection $\hat{y}_s(\theta, \rho)$ of each one $l_{(\theta, \rho)} : y \sin \theta + x \cos \theta = \rho$ in the X-rays L_s by a summation operator as below:

$$\hat{y}_s(\theta, \rho) = \sum_{(x, y) \in l_{(\theta, \rho)}} f_{\Theta}(x, y), \quad (4)$$

where $\theta = \{\theta_i\}_{i=1}^K$ are the sparse projection views and $\rho = \{\rho_j\}_{j=1}^M$ are the positions of X-rays in the detector.

Since the summation operator (Equation 4) is differentiable, the neural network used for parameterizing the implicit function f_{Θ} can be optimized by using back-propagation gradient decent algorithm to minimize the loss between the predicted projection $\hat{y}_s(\theta, \rho)$ and the real projection $\mathbf{y}_s(\theta, \rho)$ from the SV sinogram \mathbf{y}_s . In this work, we employ ℓ_1 norm as the loss function, which is defined as below:

$$\mathcal{L} = \frac{1}{k * m} \sum_{i=1}^k \sum_{j=1}^m |\mathbf{y}_s(\theta_i, \rho_j) - \hat{y}_s(\theta_i, \rho_j)|, \quad (5)$$

where k and m are respectively the number of sampled projection views and the sampled X-rays per view at each training iteration.

C. Re-projection Reconstruction

Figure 1 B shows the workflow of the proposed re-projection reconstruction strategy, in which the learned implicit function f_{Θ} is used to generate the DV sinogram $\hat{y}_d \in \mathbb{R}^{K_d \times M}$ and then the final high-quality CT image \hat{x}

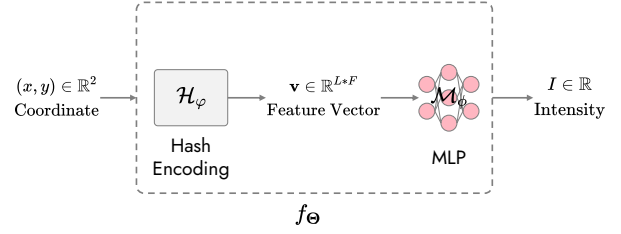


Fig. 3. The architecture of the neural network used for parameterizing the implicit function f_{Θ} , which consists of the hash encoding [35] and a three-layers MLP.

is reconstructed from the DV sinogram. More specifically, we first build $K_d * M$ X-rays L_d from K_d dense projection views (*i.e.*, M X-rays per view). Then, the spatial coordinates (x, y) of the sample points along the DV X-rays L_d are fed into the learned function to predict the corresponding image intensities $I = f_{\Theta}(x, y)$. Similarly, the projection \hat{y}_d of the X-rays L_d are also calculated by the summation operator (Equation 4). The DV sinogram \hat{y}_d is thus generated. Inspired by the data consistency in MRI acceleration reconstruction [36], we combine the estimated DV sinogram \hat{y}_d with the acquired SV sinogram \mathbf{y}_s to generate the final DV sinogram. In particular, we replace the projection profiles at the corresponding views in the DV sinogram \hat{y}_d with the SV sinogram \mathbf{y}_s . Finally, we apply FBP [10] on the final DV sinogram to reconstruct the artifacts-free CT image.

D. Network Architecture

As shown in Figure 3, the network used for learning the implicit function f_{Θ} consists of an encoding module (via hash encoding [35]) and a three-layers MLP. The network maps the input coordinate (x, y) to a feature vector $\mathbf{v} \in \mathbb{R}^{L \times F}$ and then converts the feature vector \mathbf{v} to the image intensity I . Formally, this process can be expressed as below:

$$I = \mathcal{M}_{\phi}(\mathbf{v}), \quad \mathbf{v} = \mathcal{H}_{\phi}(x, y), \quad (6)$$

where ϕ and φ represent respectively the trainable parameters of the MLP and hash encoding. They are simultaneously optimized to estimate the implicit function f_{Θ} .

1) *Hash Encoding*: The universal approximation theorem [37] proved that a pure MLP could approximate any complicated function theoretically. However, fitting high-frequency signals via the pure MLP is practically very difficult due to the spectral bias problem [33], [34]. To alleviate the issue, many encoding strategies [6], [9], [27], [35] have been proposed to map low-dimensional inputs into high-dimensional feature vectors, which allows the subsequent MLP to capture high-frequency components easily and thus reduce approximation error. In SCOPE, we adopt recent hash encoding. Unlike pre-defined encoding rules (*e.g.*, position encoding [27]), hash encoding assigns a trainable feature for each input coordinate. This adaptive encoding strategy is task-specific, which benefit from using a shallow MLP while achieving powerful fitting ability. For a coordinate grid of $N \times N$, hash encoding first builds multi-resolution of L levels feature maps $\{\mathbf{V}_i\}_{i=1}^L$. Here

TABLE II
HYPER-PARAMETERS OF THE HASH ENCODING [35] USED IN SCOPE.

Hyper-Parameter	Symbol	Value
Number of levels	L	8
Hash table size	T	2^{24}
Number of feature dimensions per entry	F	8
Coarsest resolution	N_{\min}	2
Finest resolution	N_{\max}	256

$\mathbf{V}_i \in \mathbb{R}^{N_i \times N_i \times F}$ is the feature map at the i -th level, where each element is a trainable feature vector of F length. Then, each feature map \mathbf{V}_i is mapped into a hash table of T size to reduce memory footprint. After the hash table construction, given input coordinate (x, y) , we compute its feature vector $\mathbf{v}_i \in \mathbb{R}^F$ at the i -th level via trilinear interpolation. Then, we concatenate L feature vectors $\{\mathbf{v}_i\}_{i=1}^L$ to produce the final feature vector $\mathbf{v} \in \mathbb{R}^{L \times F}$. More details about the hash encoding can be referred to [35]. Table II demonstrates the hyper-parameters of the hash encoding used in our SCOPE model.

2) *Three-Layers MLP*: After the hash encoding, the 2D input coordinate $(x, y) \in \mathbb{R}^2$ is encoded to the high-dimensional feature vector $\mathbf{v} \in \mathbb{R}^{L \times F}$. Then, a three-layers MLP is used to convert the feature vector \mathbf{v} to the image intensity I . The two hidden layers in the MLP have 64 neurons and are followed by ReLU activation and the output layer is followed by Sigmoid activation.

E. Training Parameters

For the training of the proposed SCOPE model, at each iteration, we first randomly sample 3 ones (*i.e.*, $k = 3$ in Equation 5) from sparse projection views $\{\theta_i\}_{i=1}^K$ and then randomly sample 10 ones (*i.e.*, $m = 10$ in Equation 5) from M X-rays per view. We adopt Adam optimizer [38] to minimize the ℓ_1 loss function and the hyper-parameters of the Adam are as follows: $\beta_1 = 0.9$, $\beta_2 = 0.999$, $\epsilon = 10^{-8}$. The initial learning rate is 10^{-3} and decays by a factor of 0.5 per 500 epochs. The total number of training epochs is 5000, which only takes about 5 minutes on a single NVIDIA RTX 3060 GPU. It is worth noting that all the training parameters above are the same for different cases, such as different types of X-ray beam and input views.

III. EXPERIMENTS

To evaluate the proposed SCOPE model, we perform the following three experiments: (i) We investigate the effectiveness of the re-projection reconstruction strategy; (ii) We validate the effectiveness of the hash encoding [35]; (iii) We compare our SCOPE with other five reconstruction methods quantitatively and qualitatively.

A. Dataset & Pre-processing

1) *AAPM dataset*: Based on the normal dose part of the 2016 low-dose CT challenge AAPM dataset¹ that consists of

¹<https://www.aapm.org/GrandChallenge/LowDoseCT/>

TABLE III
HYPER-PARAMETERS OF THE FOUR BUILT-IN FUNCTIONS IN MATLAB USED FOR DATA SIMULATION.

Function	Hyper-parameter	Value
radon	theta	$\{(i-1) \times 180/k\}_{i=1}^k$
iradon	theta output_size	$\{(i-1) \times 180/k\}_{i=1}^k$ $h \times w$
fanbeam	D	$\sqrt{h^2 + w^2}$
	FanRotationIncrement	$360/k$
	FanSensorSpacing	0.1
ifanbeam	D	$\sqrt{h^2 + w^2}$
	FanRotationIncrement	$360/k$
	FanSensorSpacing	0.1
	OutputSize	$h \times w$

* k is the number of projection views and $h \times w$ are the size of raw slice.

twelve 3D CT volumes acquired from twelve subjects, the AAPM dataset used in our experiments is built. Specifically, we extract 1171 2D slices from the 3D CT volumes on axial view and then split these slices into three parts: 1069 slices from ten subjects in training set, 98 slices from one subject in validation set, and 4 slices from one subject in test set. *The training and validation sets are only prepared for optimizing two supervised CNN-based baselines (FBPConvNet [16] and TF U-Net [17]), while other methods (FBP [10], CoIL [9], GRFF [6], and our SCOPE) directly recover the corresponding high-quality CT image from the single SV sinogram.*

2) *COVID-19 dataset*: COVID-19 dataset [39] is a large-scale CT dataset, which consists of 3D CT volumes from 1000+ patients with confirmed COVID-19 infections. A 3D CT volume of the COVID-19 dataset is employed as an additional test data. We select 4 slices from the volume on axial view as 4 test samples.

3) *Dataset Simulation*: For the parallel and fan X-ray beam SVCT reconstruction, we follow the strategies in [16], [17], [20] to simulate the pairs of low-quality and high-quality CT images. Specifically, we first generate the sinograms of different views (720, 120, 90, and 60) by projecting the raw slices using the built-in functions `radon` and `fanbeam` in MATLAB, respectively. Then, we transfer the sinograms back to CT images using the built-in functions `iradon` and `ifanbeam` in MATLAB, respectively. Detailed hyper-parameters of the four functions are demonstrated in Table III. The images reconstructed from 720 views are used for Ground Truth (GT), while the images reconstructed from 120, 90, and 60 views are used for input images corresponding to three different factors $6\times$, $8\times$, and $12\times$. Note that the parallel and fan X-ray beam SVCT are considered as two independent reconstruction tasks. Thus, all the training and test processes are solely conducted.

B. Compared Methods & Evaluation Metrics

1) *Compared Methods*: We compare the proposed SCOPE model with five SVCT reconstruction methods: (i) FBP [10], a classical analytical reconstruction algorithm; (ii) CoIL [9], an INR-based method. Since the output of CoIL is the DV sinogram, we thus apply FBP on the generated DV sinogram

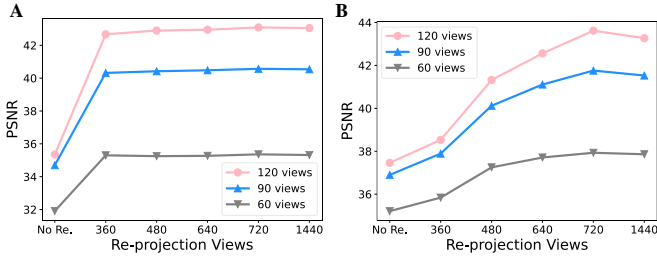


Fig. 4. Quantitative results of the proposed SCOPE model with two reconstruction strategies on the COVID-19 dataset for *parallel* (A) and *fan* (B) X-ray beam SVCT of 60, 90, and 120 views.

to reconstruct the CT image; (iii) GRFF [6], an INR-based method with Gaussian random Fourier feature encoding strategy; (iv) FBPCovNet [16], a supervised DL method based on U-Net [23]; (v) TF U-Net [17], a supervised DL method based on Tigh Frame U-Net. We train FBPCovNet and TF U-Net on the training set of the AAPM dataset through Adam optimizer [38] with a mini-batch of 8. The learning rate starts form 10^{-3} from 10^{-6} , which gradually decreases over each training epoch. The total training epochs are set as 500 and the best model is saved by checkpoints during the training process. The two INR-based methods (CoIL and GRFF) are implemented following the original papers.

2) *Evaluation Metrics*: To quantitatively measure the performance of the compared methods, we calculate Peak Signal-to-Noise Ratio (PSNR) and Structural Similarity Index Measure (SSIM) [40]. They are the two most used objective image quality metrics in low-level vision tasks. PSNR is defined based on pixel-by-pixel distance while SSIM measures structural similarity using the mean and variance of images. Moreover, we also compute LPIPS [41], a DL-based objective perceptual similarity metric.

C. Effectiveness of Re-projection Reconstruction

First, we investigate the effectiveness of the proposed re-projection strategy. After the network training, we adopt the following two strategies to recover the final CT image: (i) No Re-projection, we directly feed all the coordinates into the MLP to produce the corresponding image intensities; (ii) K_d Re-projection Views, we employ the MLP to generate the DV sinograms (360, 480, 640, 720, and 1440 views) and then apply FBP algorithm [10] on the DV sinogram to reconstruct the CT images.

Figure 4 shows the quantitative results on the COVID-19 dataset for parallel and fan X-ray beam SVCT of 60, 90, and 120 views. Overall, the re-projection reconstruction strategy significantly improves performance for all the cases. For example, PSNR improves about 3 dB for fan X-ray beam SVCT reconstruction of 60 views. More importantly, there is a common trend in all the cases: The model performance gradually increase when the re-projection views increase from 360 to 720 but slightly decrease when the re-projection views increase from 720 to 1440. Our explanation is: (i) The projections of views less than 720 are not dense enough. Although the intensity mutation of the highest frequency are completely

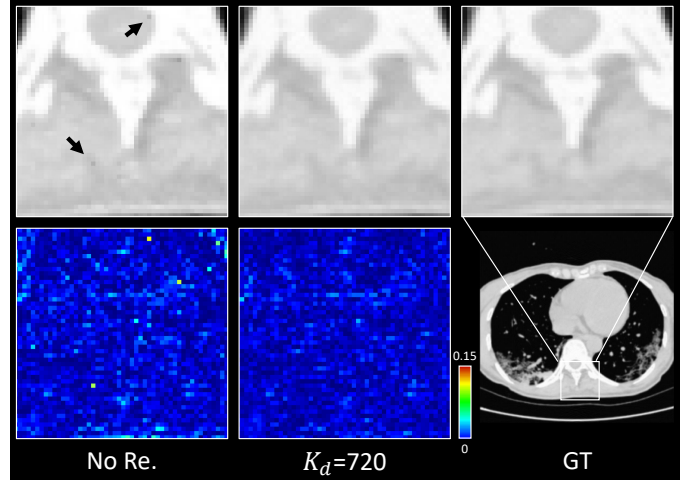


Fig. 5. Qualitative results (Zoom regions and their absolute error maps) of the proposed SCOPE model with two reconstruction strategies on a test sample (#80) from the COVID-19 dataset for *fan* X-ray beam SVCT of 90 views.

TABLE IV
QUALITATIVE RESULTS (PSNR/SSIM/LPIPS) OF THE SCOPE MODEL WITH THREE ENCODING MODULES ON THE COVID-19 DATASET FOR *parallel* AND *fan* X-RAYS BEAM SVCT OF 60, 90, AND 120 VIEWS.

X-ray	Views	No En.	Pos. En.	Ha. En.
Parallel	60	27.52/0.8378/0.1414	35.19/0.8870/0.0152	35.36/0.9512/0.0196
	90	28.48/0.8632/0.1166	38.65/0.9207/0.0046	40.57/0.9807/0.0040
	120	29.30/0.8831/0.0991	40.05/0.9294/0.0049	43.09/0.9872/0.0023
Fan	60	24.10/0.7256/0.1851	36.27/0.9539/0.0115	37.93/0.9727/0.0067
	90	25.97/0.7828/0.1586	39.56/0.9760/0.0100	41.76/0.9854/0.0023
	120	26.51/0.8017/0.1444	41.73/0.9839/0.0049	43.62/0.9888/0.0015

removed, the image details of sub-high frequency are also partially lost. (ii) The projections of views more than 720 are over-dense, which results in incomplete removal of the intensity mutation of the highest frequency and obtains the sub-optimal performance. Therefore, we set the re-projection views as $K_d = 720$ in this paper, but it is worth noting that the parameter may need to be adjusted for specific cases. Figure 5 demonstrates the qualitative results on a test sample #80 for fan X-ray beam SVCT of 90 views. We observe that the image from the direct reconstruction (*i.e.*, No Re.) contains a lot of noises, while the results from our re-projection strategy are clear and closer to GT images.

D. Effectiveness of Hash Encoding

Next, we validate the effectiveness of the hash encoding [35]. The proposed SCOPE model with three different encoding modules are compared: (i) No Encoding, a pure nine-layers MLP without any encoding module; (ii) Position Encoding, a nine-layers MLP with the position encoding [27]; (iii) Hash Encoding, a three-layers MLP with the hash encoding.

Table IV shows the quantitative results on the COVID-19 dataset for parallel and fan X-ray beam SVCT of 60, 90, and 120 views. From the results, we see that compared with no encoding, both the position encoding and hash encoding significantly improve the model performance in terms of all the three metrics for all the cases. For example, PSNR respectively improve 13.59 dB (39.56 vs. 25.97) and 15.79 dB (41.76

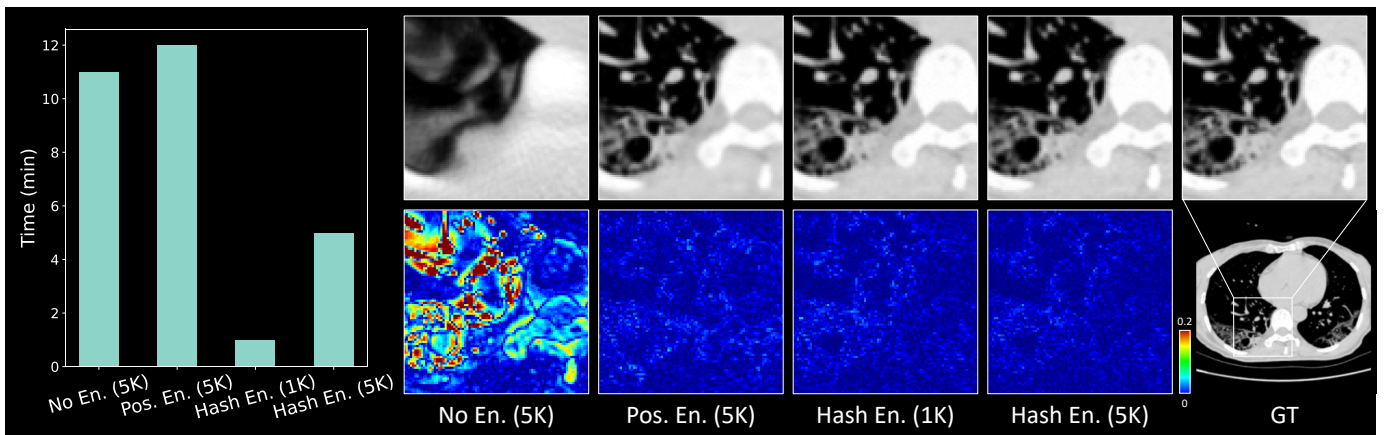


Fig. 6. Qualitative results (Zoom regions and their absolute error maps) of our SCOPE model with three encoding modules on a test sample (#95) of the COVID-19 dataset for *fan* X-ray beam SVCT of 90 views. Here the numbers in parentheses denote training epochs.

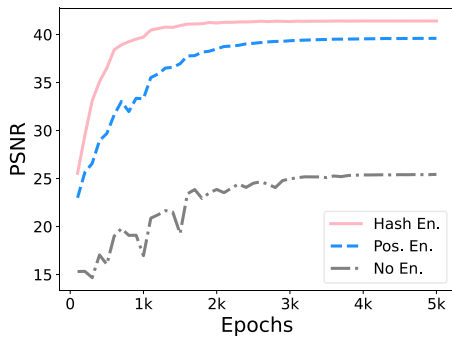


Fig. 7. Performance curves of SCOPE with three encoding modules over training epochs on a test sample (#95) of the COVID-19 dataset for *fan* X-ray beam SVCT of 90 views.

vs. 25.97) for *fan* X-ray beam SVCT reconstruction of 90 views. This is due to the spectral bias problem [33], [34] (*i.e.*, a pure MLP is biased toward learning low-frequency signals during the practical training). Thus, encoding modules are critical for improving the MLP’s ability to learn high-frequency signals. Besides, we observe that the hash encoding slightly outperforms the position encoding for the most cases. For instance, PSNR improves 1.66 dB (37.93 vs. 36.27) for *fan* X-ray beam SVCT reconstruction of 60 views. Figure 6 shows the qualitative results on a test sample (#95) for *fan* X-ray beam SVCT reconstruction of 90 views. Overall, the hash encoding achieves the best image quality and the fastest reconstruction speed. benefiting from the shallower MLP (3 vs. 9), the hash encoding takes only about 1min to obtain the same performance as the position encoding. However, the position encoding takes 12mins, which is about 12 \times acceleration. We also show the performance curves of the SCOPE model with the three encoding modules over training epochs in Figure 7. Obviously, the hash encoding produces the best performance.

E. Comparison with Other Methods

We compare the proposed SCOPE model with the five baselines on the AAPM and COVID-19 datasets for parallel

and *fan* X-ray beam SVCT reconstruction. Since FBPCNet [16] and TF U-Net [17] are supervised DL methods, we train them on the training set of the AAPM dataset. Other four methods (FBP [10], CoIL [9], GRFF [6], and our SCOPE model) are image-specific and thus they direct reconstruct the corresponding high-quality CT image from each SV sinogram. Note that the parallel and *fan* X-ray beam SVCT are considered two independent reconstruction tasks and thus all the training and test processes are solely conducted.

1) *Parallel X-ray Beam SVCT*: Table V shows the quantitative results of the compared methods on the two datasets for parallel X-ray beam SVCT of 60, 90, and 120 views. On the AAPM dataset, our SCOPE produces the best performance for most cases. Compared with the two supervised DL methods (FBPCNet [16] and TF U-Net [17]), SCOPE also obtains minor performance improvements. For instance, PSNR respectively improve 0.27 dB (42.18 vs. 41.95) and 0.44 dB (42.18 vs. 41.74) when 90 input views. On the COVID-19 dataset, we, however, observe that FBPCNet and TF U-Net suffer from severe performance drops. This is mainly due to the domain shift problem (*i.e.*, the training and test data do not share the same distribution). In comparison, our SCOPE model still produces excellent reconstruction results on the COVID-19 data because it is image-specific. For example, the difference in PSNR between SCOPE and FBPCNet is up to +3.92 dB (40.57 vs. 36.65) when 90 input views. Figure 8 & 9 show the qualitative results on two test samples (#109 and #90) from the two datasets for parallel X-ray beam SVCT of 90 views. On the test sample #109 from the AAPM dataset, both FBP [10] and CoIL [9] can not produce the satisfactory results, which still include a lot of streaking artifacts. GRFF [6] yields the smooth result that lost some image details. In comparison, FBPCNet, TF U-Net, and SCOPE all recover the desirable images that are hardly distinguished from GT image. On the test sample #90 from the COVID-19 dataset, the two supervised models obtain sub-optimal results including moderate streaking artifacts, while our SCOPE model still produces high-quality image that is closest to GT image.

2) *Fan X-ray Beam SVCT*: Table VI demonstrates the quantitative results of the compared methods on the two

TABLE V
 QUANTITATIVE RESULTS (PSNR/SSIM/LPIPS) OF DIFFERENT METHODS ON THE AAPM AND COVID-19 DATASETS FOR *parallel* X-RAYS BEAM SVCT OF 60, 90, AND 120 VIEWS.

Dataset	Views	FBP	CoLL	GRFF	FBPConvNet	TF U-Net	SCOPE (Ours)
AAPM	60	19.98/0.2791/0.4536	19.60/0.5587/0.1229	35.99/0.9448/0.0236	38.66/0.9392/0.0124	38.67/0.9388/0.0134	38.05/0.9596/0.0182
	90	24.40/0.4328/0.3424	22.37/0.6937/0.0747	38.89/0.9664/0.0139	41.95/0.9557/0.0078	41.74/0.9587/0.0079	42.18/0.9794/0.0066
	120	28.30/0.5869/0.2567	24.99/0.7909/0.0454	39.71/0.9716/0.0123	44.14/0.9644/0.0047	43.86/0.9688/0.0043	44.33/0.9860/0.0037
COVID-19	60	22.53/0.4979/0.3353	20.31/0.5995/0.1085	33.76/0.9494/0.0209	32.87/0.9236/0.0256	32.86/0.9297/0.0214	35.36/0.9512/0.0196
	90	27.56/0.6722/0.2168	23.26/0.7516/0.0511	35.51/0.9676/0.0128	36.65/0.9563/0.0110	36.59/0.9571/0.0106	40.57/0.9807/0.0040
	120	31.60/0.8025/0.1174	25.96/0.8434/0.0248	35.95/0.9702/0.0120	38.40/0.9661/0.0088	38.71/0.9675/0.0078	43.09/0.9872/0.0023

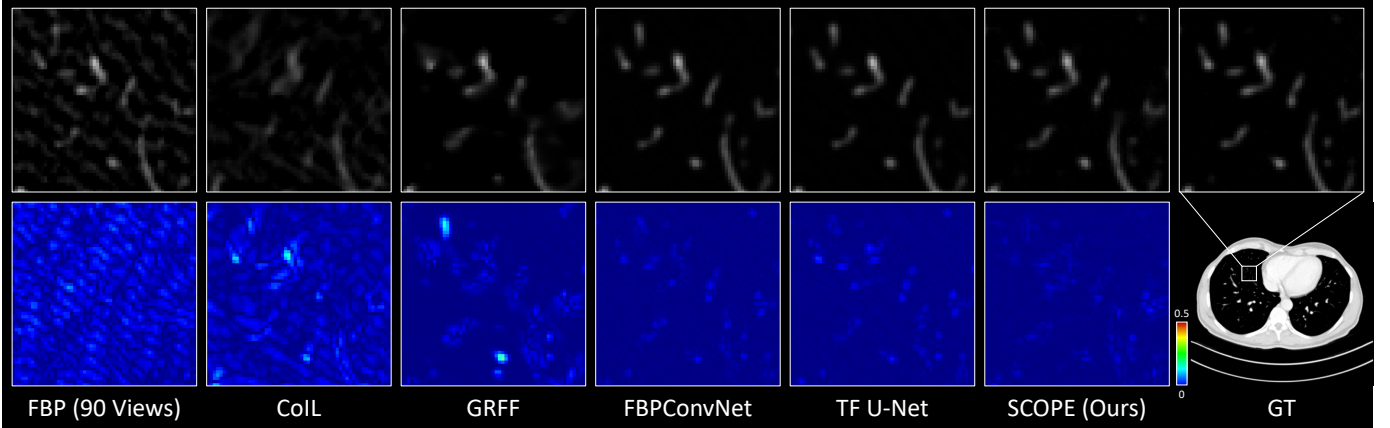


Fig. 8. Qualitative results (Zoom regions and their absolute error maps) of different methods on a test sample (#109) of the AAPM dataset for *parallel* X-ray beam SVCT of 90 views.

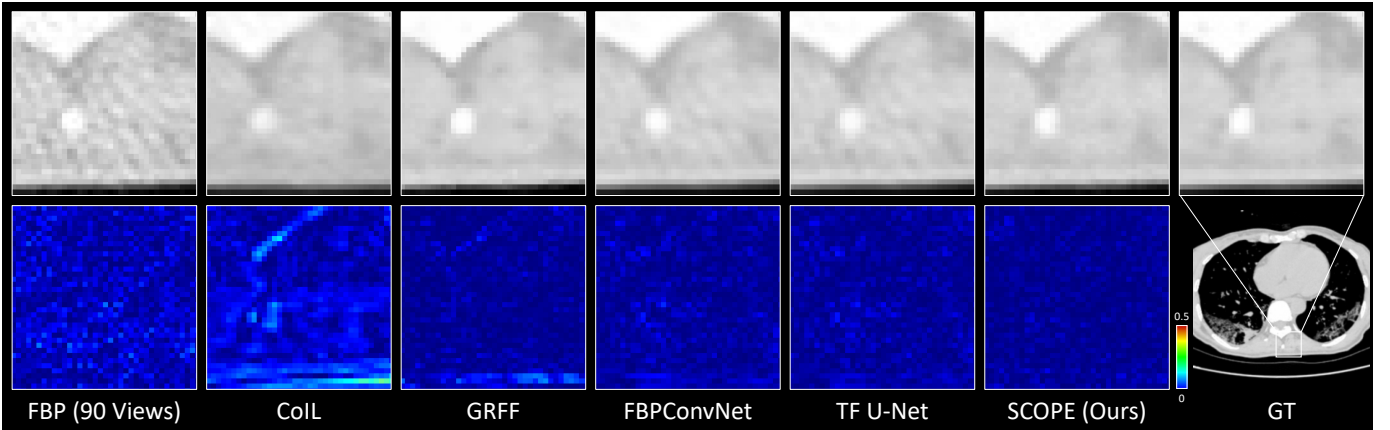


Fig. 9. Qualitative results (Zoom regions and their absolute error maps) of different methods on a test sample (#90) of the COVID-19 dataset for *parallel* X-ray beam SVCT of 90 views.

datasets for fan X-ray beam SVCT of 60, 90, and 120 views. We observe that the proposed SCOPE and GRFF [6] respectively produce the best and second-best performance in terms of all the three metrics for all the cases. For example, on the AAPM dataset for 90 input views, SCOPE and GRFF respectively achieve 40.92 dB and 37.54 dB, while TF U-Net [17] only obtains 32.47 dB in terms of PSNR. It is not common that FBPConvNet [16] and TF U-Net cannot produce the satisfactory performance on the AAPM dataset although they are trained on the AAPM dataset. We guess that, for learning the end-to-end mapping as in the supervised DL methods, the fan X-ray beam CT is a more difficult task than the parallel X-ray beam CT when same input views. In our

experiments, for the sinograms of the same projection views, the results of the fan X-ray CT include more severe streaking artifacts than that of the parallel X-ray CT after applying the FBP algorithm [10]. While FBPConvNet [16] and TF U-Net [17] directly learn the inverse mapping from the artifacts-corrupted inputs to the artifacts-free outputs. Therefore, they are not expected to perform as well in the fan X-ray CT as in the parallel X-ray CT. In contrast, GRFF [6] and SCOPE train neural network to learn the implicit function of the unknown CT image by computing the loss on the SV sinogram (*i.e.*, they do not manipulate image information directly). Thus, they all work well for different types of X-ray beams. Figure 10 & 11 show the qualitative results on two test samples (#104

TABLE VI
 QUANTITATIVE RESULTS (PSNR/SSIM/LPIPS) OF DIFFERENT METHODS ON THE AAPM AND COVID-19 DATASETS FOR *fan* X-RAYS BEAM SVCT OF 60, 90, AND 120 VIEWS.

Dataset	Views	FBP	CoIL	GRFF	FBPConvNet	TF U-Net	SCOPE (Ours)
AAPM	60	13.74/0.1224/0.6210	19.30/0.4546/0.1882	34.48/0.9268/0.0455	28.72/0.8622/0.0533	28.31/0.8274/0.0605	37.93/0.9560/0.0131
	90	16.40/0.1882/0.5425	22.10/0.5626/0.1455	37.54/0.9533/0.0297	31.95/0.9103/0.0360	32.47/0.8910/0.0405	40.92/0.9719/0.0076
	120	19.34/0.2721/0.4694	24.64/0.6509/0.1142	38.88/0.9621/0.0244	34.56/0.9337/0.0285	34.94/0.9226/0.0309	42.76/0.9788/0.0049
COVID-19	60	15.15/0.2230/0.5010	19.55/0.4557/0.2004	34.00/0.9401/0.0208	23.03/0.7274/0.1368	23.12/0.7044/0.1490	37.93/0.9727/0.0067
	90	18.87/0.3642/0.4108	22.53/0.6013/0.1290	36.31/0.9607/0.0100	25.58/0.8030/0.1079	25.05/0.7795/0.1135	41.76/0.9854/0.0023
	120	21.95/0.4832/0.3477	25.08/0.7155/0.0821	37.16/0.9679/0.0110	27.28/0.8443/0.0811	26.43/0.8169/0.0887	43.62/0.9888/0.0015

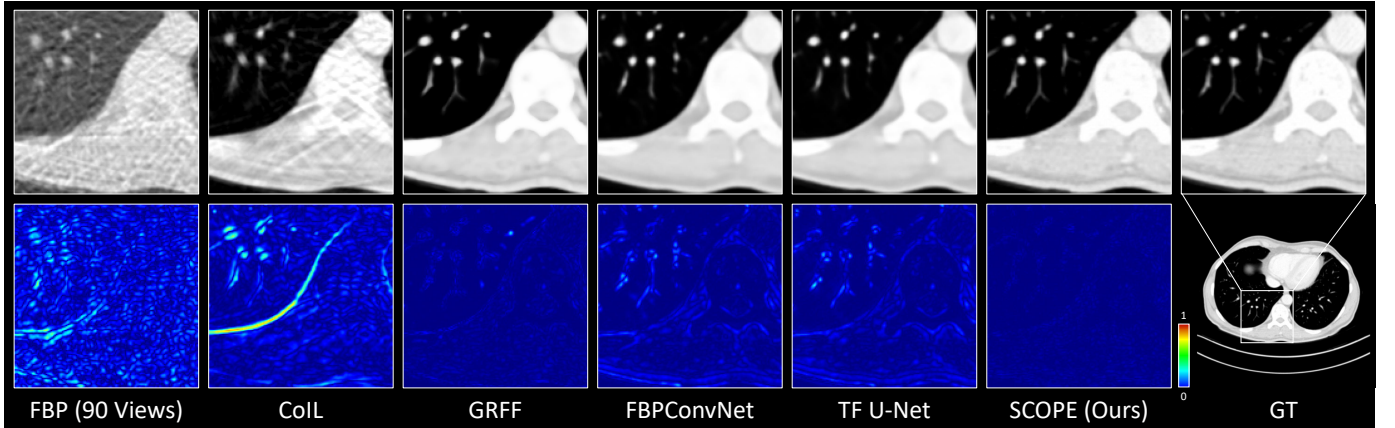


Fig. 10. Qualitative results (Zoom regions and their absolute error maps) of different methods on a test sample (#104) of the AAPM dataset for *fan* X-ray beam SVCT of 90 views.

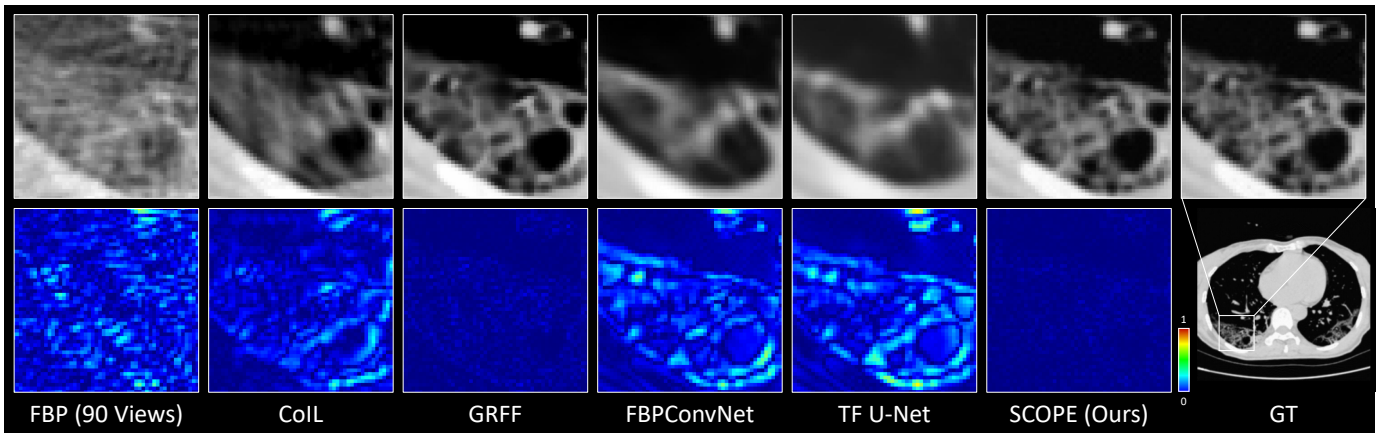


Fig. 11. Qualitative results (Zoom regions and their absolute error maps) of different methods on a test sample (#95) of the COVID-19 dataset for *fan* X-ray beam SVCT of 90 views.

and #95) from the two datasets for *fan* X-ray beam SVCT reconstruction of 90 views. We see that the four compared methods do not recover the good results. The results from FBP algorithm [10] and CoIL [9] include severe streaking artifacts, while FBPConvNet [16] and TF U-Net [17] produce the overly smooth results. GRFF [6] obtains the second-best results that lost some image details. Only the proposed SCOPE removes streaking artifacts greatly and preserves fine image details well.

IV. CONCLUSION

In this work, we propose SCOPE, a self-supervised INR-based method for SVCT reconstruction. Like previous INR

works [6], SCOPE represents the desired CT image as an implicit continuous function and trains a neural network to learn the implicit function by minimizing predicted errors on the acquired SV sinogram. Benefiting from image continuity prior imposed by the implicit function and neural network architecture prior, the function can be estimated. However, the solution is not optimal due to the overfitting problem. To this end, we propose a simple and effective re-projection strategy that greatly improves the resulting CT image quality. Besides, we adopt the recent hash encoding [35] into our SCOPE to accelerate the model training greatly. Experimental results on two publicly available datasets indicate that the proposed SCOPE model is not only superior to two last INR-based

methods, but also outperforms two well-known supervised CNN-based methods, qualitatively and quantitatively.

REFERENCES

- [1] G. Wang, H. Yu, and B. De Man, "An outlook on x-ray ct research and development," *Medical physics*, vol. 35, no. 3, pp. 1051–1064, 2008.
- [2] H. Chen, Y. Zhang, M. K. Kalra, F. Lin, Y. Chen, P. Liao, J. Zhou, and G. Wang, "Low-dose ct with a residual encoder-decoder convolutional neural network," *IEEE transactions on medical imaging*, vol. 36, no. 12, pp. 2524–2535, 2017.
- [3] C. Long, H. Xu, Q. Shen, X. Zhang, B. Fan, C. Wang, B. Zeng, Z. Li, X. Li, and H. Li, "Diagnosis of the coronavirus disease (covid-19): rrt-per or ct?" *European journal of radiology*, vol. 126, p. 108961, 2020.
- [4] E. Hall and D. Brenner, "Cancer risks from diagnostic radiology," *The British journal of radiology*, vol. 81, no. 965, pp. 362–378, 2008.
- [5] D. J. Brenner and E. J. Hall, "Computed tomography—an increasing source of radiation exposure," *New England journal of medicine*, vol. 357, no. 22, pp. 2277–2284, 2007.
- [6] M. Tancik, P. Srinivasan, B. Mildenhall, S. Fridovich-Keil, N. Raghavan, U. Singhal, R. Ramamoorthi, J. Barron, and R. Ng, "Fourier features let networks learn high frequency functions in low dimensional domains," *Advances in Neural Information Processing Systems*, vol. 33, pp. 7537–7547, 2020.
- [7] G. Zang, R. Idoughi, R. Li, P. Wonka, and W. Heidrich, "Intratomo: Self-supervised learning-based tomography via sinogram synthesis and prediction," in *Proceedings of the IEEE/CVF International Conference on Computer Vision*, 2021, pp. 1960–1970.
- [8] L. Shen, J. Pauly, and L. Xing, "Nerp: Implicit neural representation learning with prior embedding for sparsely sampled image reconstruction," *IEEE Transactions on Neural Networks and Learning Systems*, pp. 1–13, 2022.
- [9] Y. Sun, J. Liu, M. Xie, B. Wohlberg, and U. S. Kamilov, "Coil: Coordinate-based internal learning for tomographic imaging," *IEEE Transactions on Computational Imaging*, vol. 7, pp. 1400–1412, 2021.
- [10] A. C. Kak and M. Slaney, *Principles of computerized tomographic imaging*. SIAM, 2001.
- [11] E. Y. Sidky, C.-M. Kao, and X. Pan, "Accurate image reconstruction from few-views and limited-angle data in divergent-beam ct," *Journal of X-ray Science and Technology*, vol. 14, no. 2, pp. 119–139, 2006.
- [12] K. Kim, J. C. Ye, W. Worstell, J. Ouyang, Y. Rakvongthai, G. El Fakhri, and Q. Li, "Sparse-view spectral ct reconstruction using spectral patch-based low-rank penalty," *IEEE transactions on medical imaging*, vol. 34, no. 3, pp. 748–760, 2014.
- [13] E. Y. Sidky and X. Pan, "Image reconstruction in circular cone-beam computed tomography by constrained, total-variation minimization," *Physics in Medicine & Biology*, vol. 53, no. 17, p. 4777, 2008.
- [14] L. I. Rudin, S. Osher, and E. Fatemi, "Nonlinear total variation based noise removal algorithms," *Physica D: nonlinear phenomena*, vol. 60, no. 1-4, pp. 259–268, 1992.
- [15] R. Liu, Y. Sun, J. Zhu, L. Tian, and U. Kamilov, "Zero-shot learning of continuous 3d refractive index maps from discrete intensity-only measurements," *arXiv preprint arXiv:2112.00002*, 2021.
- [16] K. H. Jin, M. T. McCann, E. Froustey, and M. Unser, "Deep convolutional neural network for inverse problems in imaging," *IEEE Transactions on Image Processing*, vol. 26, no. 9, pp. 4509–4522, 2017.
- [17] Y. Han and J. C. Ye, "Framing u-net via deep convolutional framelets: Application to sparse-view ct," *IEEE transactions on medical imaging*, vol. 37, no. 6, pp. 1418–1429, 2018.
- [18] Z. Zhang, X. Liang, X. Dong, Y. Xie, and G. Cao, "A sparse-view ct reconstruction method based on combination of densenet and deconvolution," *IEEE transactions on medical imaging*, vol. 37, no. 6, pp. 1407–1417, 2018.
- [19] H. Lee, J. Lee, H. Kim, B. Cho, and S. Cho, "Deep-neural-network-based sinogram synthesis for sparse-view ct image reconstruction," *IEEE Transactions on Radiation and Plasma Medical Sciences*, vol. 3, no. 2, pp. 109–119, 2018.
- [20] T. Shen, X. Li, Z. Zhong, J. Wu, and Z. Lin, "R²-net: Recurrent and recursive network for sparse-view ct artifacts removal," in *International Conference on Medical Image Computing and Computer-Assisted Intervention*. Springer, 2019, pp. 319–327.
- [21] Y. Li, K. Li, C. Zhang, J. Montoya, and G.-H. Chen, "Learning to reconstruct computed tomography images directly from sinogram data under a variety of data acquisition conditions," *IEEE transactions on medical imaging*, vol. 38, no. 10, pp. 2469–2481, 2019.
- [22] Q. Ding, H. Ji, H. Gao, and X. Zhang, "Learnable multi-scale fourier interpolation for sparse view ct image reconstruction," in *International Conference on Medical Image Computing and Computer-Assisted Intervention*. Springer, 2021, pp. 286–295.
- [23] O. Ronneberger, P. Fischer, and T. Brox, "U-net: Convolutional networks for biomedical image segmentation," in *International Conference on Medical image computing and computer-assisted intervention*. Springer, 2015, pp. 234–241.
- [24] J. J. Park, P. Florence, J. Straub, R. Newcombe, and S. Lovegrove, "Deepsdf: Learning continuous signed distance functions for shape representation," in *Proceedings of the IEEE/CVF Conference on Computer Vision and Pattern Recognition*, 2019, pp. 165–174.
- [25] Z. Chen and H. Zhang, "Learning implicit fields for generative shape modeling," in *Proceedings of the IEEE/CVF Conference on Computer Vision and Pattern Recognition*, 2019, pp. 5939–5948.
- [26] L. Mescheder, M. Oechsle, M. Niemeyer, S. Nowozin, and A. Geiger, "Occupancy networks: Learning 3d reconstruction in function space," in *Proceedings of the IEEE/CVF Conference on Computer Vision and Pattern Recognition*, 2019, pp. 4460–4470.
- [27] B. Mildenhall, P. P. Srinivasan, M. Tancik, J. T. Barron, R. Ramamoorthi, and R. Ng, "Nerf: Representing scenes as neural radiance fields for view synthesis," in *European conference on computer vision*. Springer, 2020, pp. 405–421.
- [28] K. Zhang, G. Riegler, N. Snavely, and V. Koltun, "Nerf++: Analyzing and improving neural radiance fields," *arXiv preprint arXiv:2010.07492*, 2020.
- [29] D. Rebain, W. Jiang, S. Yazdani, K. Li, K. M. Yi, and A. Tagliasacchi, "Derf: Decomposed radiance fields," in *Proceedings of the IEEE/CVF Conference on Computer Vision and Pattern Recognition*, 2021, pp. 14 153–14 161.
- [30] Y. Chen, S. Liu, and X. Wang, "Learning continuous image representation with local implicit image function," in *Proceedings of the IEEE/CVF Conference on Computer Vision and Pattern Recognition*, 2021, pp. 8628–8638.
- [31] J. Tang, X. Chen, and G. Zeng, "Joint implicit image function for guided depth super-resolution," in *Proceedings of the 29th ACM International Conference on Multimedia*, 2021, pp. 4390–4399.
- [32] A. W. Reed, H. Kim, R. Anirudh, K. A. Mohan, K. Champley, J. Kang, and S. Jayasuriya, "Dynamic ct reconstruction from limited views with implicit neural representations and parametric motion fields," in *Proceedings of the IEEE/CVF International Conference on Computer Vision*, 2021, pp. 2258–2268.
- [33] N. Rahaman, A. Baratin, D. Arpit, F. Draxler, M. Lin, F. Hamprecht, Y. Bengio, and A. Courville, "On the spectral bias of neural networks," in *International Conference on Machine Learning*. PMLR, 2019, pp. 5301–5310.
- [34] Z.-Q. J. Xu, Y. Zhang, T. Luo, Y. Xiao, and Z. Ma, "Frequency principle: Fourier analysis sheds light on deep neural networks," *arXiv preprint arXiv:1901.06523*, 2019.
- [35] T. Müller, A. Evans, C. Schied, and A. Keller, "Instant neural graphics primitives with a multiresolution hash encoding," *arXiv preprint arXiv:2201.05989*, 2022.
- [36] B. Yaman, S. A. H. Hosseini, S. Moeller, J. Ellermann, K. Uğurbil, and M. Akçakaya, "Self-supervised learning of physics-guided reconstruction neural networks without fully sampled reference data," *Magnetic resonance in medicine*, vol. 84, no. 6, pp. 3172–3191, 2020.
- [37] K. Hornik, M. Stinchcombe, and H. White, "Multilayer feedforward networks are universal approximators," *Neural networks*, vol. 2, no. 5, pp. 359–366, 1989.
- [38] D. P. Kingma and J. Ba, "Adam: A method for stochastic optimization," *CoRR*, vol. abs/1412.6980, 2015.
- [39] S. Shakouri, M. A. Bakhshali, P. Layegh, B. Kiani, F. Masoumi, S. Ataei Nakhaei, and S. M. Mostafavi, "Covid19-ct-dataset: an open-access chest ct image repository of 1000+ patients with confirmed covid-19 diagnosis," *BMC Research Notes*, vol. 14, no. 1, pp. 1–3, 2021.
- [40] Z. Wang, A. Bovik, H. Sheikh, and E. Simoncelli, "Image quality assessment: from error visibility to structural similarity," *IEEE Transactions on Image Processing*, vol. 13, no. 4, pp. 600–612, 2004.
- [41] R. Zhang, P. Isola, A. A. Efros, E. Shechtman, and O. Wang, "The unreasonable effectiveness of deep features as a perceptual metric," in *CVPR*, 2018.